Nanoscale

PAPER

View Article Online
View Journal

Cite this: DOI: 10.1039/d6nr00916f

Received 5th March 2026,
Accepted 10th May 2026

DOI: 10.1039/d6nr00916f

rsc.li/nanoscale

Single-molecule glycan discrimination using a graphite nanopore

Chandan K. Das *[a,b] and Maria Fyta [a,b]

Glycans are fundamental biomolecules whose biological functions are encoded in subtle structural features, posing significant challenges for their analytical discrimination. In this all-atom molecular dynamics study, we demonstrate that a negatively charged graphite nanopore enables accurate single-molecule glycan detection. Glycans differing in *N*-acetylation number, *N*-acetylation pattern, and regioisomeric structure are reliably discriminated. In fact, from a mechanistic perspective, distinct ionic current signatures are traced back to species-specific spatial charge accumulation around individual glycans confined within the nanopore lumen. Moreover, under applied transmembrane voltage, the negatively charged nanopore generates electroosmotic flow, which drives glycan translocation and offers a chemically label-free approach for glycan detection.

1 Introduction and background

Glycans, composed of multiple monosaccharide units connected by glycosidic linkages, are essential biological macromolecules alongside proteins and polynucleic acids. Notably, the biological functions, particularly the molecular recognition processes of glycans and glycoconjugates (such as, glycolipids and glycoproteins), are directly associated with the structural features of sugar moieties.[1,2] For instance, the functional groups in glycans determine their chemical properties, which in turn modulate their binding affinity.[2] Variations in glycosidic linkages give rise to distinct glycan conformations, further affecting receptor binding. In addition, glycan chain length also plays a key role in biological processes such as cell adhesion and intracellular trafficking.[3] Therefore, accurate structural elucidation of glycans is vital for improving disease diagnosis[4] and advancing drug development.[5]

Unlike uniformly charged polynucleic acids and compositionally diverse proteins with heterogeneous charge distributions, glycans are generally uncharged and display extensive stereochemical diversity resulting from variations in monosaccharide composition, anomeric configuration, and glycosidic linkage. This inherent structural complexity of glycans poses significant challenges for their accurate detection and sequencing. In DNA sequencing, as well as more recently in protein sequencing, the nanopore detection technology has achieved remarkable success owing to its accurate, fast, chemical-free, and cost-effective approach.[6] In nanopore-based single-molecule sensing, an analyte translocates through the nanopore, producing characteristic changes in ionic current signals. These signal modulations can then be analyzed to infer the structural and compositional information of the analyte.

In the past few years, nanopore sequencing of glycans has been realized, primarily using biological nanopores such as α-hemolysin,[8–11] aerolysin,[12–14] *Mycobacterium smegmatis* porin A (MspA),[15–17] and outer membrane porin F (OmpF).[18] The monosaccharide isomers D-glucose and D-fructose were successfully discriminated using an engineered α-hemolysin nanopore functionalized with phenylboronic acid. Phenylboronic acid reversibly reacts with monosaccharides, prolonging their residence time within the nanopore and thereby enhancing the accuracy of saccharide detection.[8] This strategy was subsequently extended to enable the identification of nine commonly occurring monosaccharides, including D-galactose, D-mannose, D-glucose, L-sorbose, D-ribose, D-xylose, L-rhamnose, and *N*-acetyl-D-galactosamine, using the MspA biological nanopore.[15] Furthermore, MspA nanopores conjugated with a phenylboronic acid adapter have been employed to distinguish disaccharides with different glycosidic linkages.[16] Glycans with chain lengths ranging from disaccharides to pentasaccharides have also been differentiated using chemically labeled approaches based on the aerolysin nanopore.[12] More recently, label-free detection of neutrally charged polysaccharides has been successfully achieved using OmpF[18] and α-hemolysin[10] nanopores, alongside glycosidase-assisted glycan sequencing approach.[11] Collectively, these pioneering studies highlight the great potential of nanopore technologies for saccharide detection. However, the translocation of net charge-neutral glycan molecules through biological nanopores

---

[a] *Computational Biotechnology, RWTH Aachen University, Worrignerweg 3, 52074 Aachen, Germany. E-mail: c.das@biotec.rwth-aachen.de*

[b] *Center for Computational Life Sciences (CCLS), RWTH Aachen University, Pauwelsstrasse 19, 52072 Aachen, Germany*

poses a significant challenge for bio-nanopore-based glycan sequencing technologies. This limitation is circumvented in OmpF-based nanopores,[18] where the naturally charged lumen generates electro-osmotic flow (EOF) under an applied transmembrane voltage, thereby driving glycan translocation. A similar EOF-guided translocation strategy could, in principle, be achieved in charged solid-state nanopores.[19]

In contrast to biological nanopores, glycan detection with solid-state nanopores remains relatively unexplored. Recently though, Pathak and co-workers demonstrated the discrimination of monosaccharide anomers and stereoisomers with excellent sensitivity using graphene-based nanogap electrodes by integrating quantum transport measurements with artificial intelligence.[20] This approach has been further extended to also differentiate among various regioisomers.[21] Nevertheless, ionic current-based glycan detection using material-based nanopores remains an untapped frontier in nanopore analytics. In fact, though biological pores are considered more specific and can be selectively engineered,[22] solid-state materials can be better integrated with electronics and combined with different measurement modalities (ionic, electronic, optical).[23] With this in mind, we aim here to unravel the potential of solid-state nanopores in glycan detection. In the pursuit of optimal pore geometry for solid-state nanopores, the aerolysin biological nanopore has emerged as a particularly inspiring model. The aerolysin nanopore has achieved exceptional success not only in glycan sensing,[12,13] but also in resolving isomeric post-translational modifications (PTMs) in the human histone H4 protein.[24] Inspired by the charged, narrow, and nearly cylindrical pore architecture of aerolysin, we fabricated a cylindrical graphite nanopore without a constriction zone (Fig. 1). Exploiting the electrical conductivity of graphite, an external voltage was applied to the nanopore to render it negatively charged. Additionally, an independent transmembrane electric bias was applied to drive ion flow, generating ionic currents through which glycans could be discriminated. Unlike polynucleic acids such as DNA and RNA, glycan chains are typically net charge-neutral molecules. Consequently, electrophoretic forces (EPF) alone are ineffective for driving glycan translocation through a nanopore,[25] in contrast to DNA, where the negatively charged phosphate backbone enables efficient electrophoretic transport. This limitation in the case of glycans can be overcome through the use of an EOF. Previous studies demonstrated that the charged nanopore exhibits charge-exclusive ion selectivity, which gives rise to an EOF associated with a pronounced unidirectional water flow through the pore.[19,26,27] Notably, the combination of EOF acting opposite to the EPF has been shown to be effective in linearizing a protein within the pore lumen, a critical requirement for protein sequencing.[19]

Using an all-atom Molecular Dynamics (MD) approach, we unravel how the combined driving forces of EPF and EOF govern glycan translocation through the pore lumen. Within this concept, we have systematically investigated poly-*N*-acetyllactosamine glycans (see Fig. 2), which constitute the backbone of glycoconjugates such as N- and O-linked glycoproteins and glycolipids.[1] These glycans consist of repeating units in which *N*-acetylglucosamine alternates with galactose and display diverse structural variations, including differences in functional group composition, glycosidic linkage types, and chain length. Our proof-of-concept study provides comprehensive insights into the differentiation of these glycans, underscoring the capability of graphite nanopores for precise, label-free glycan discrimination.

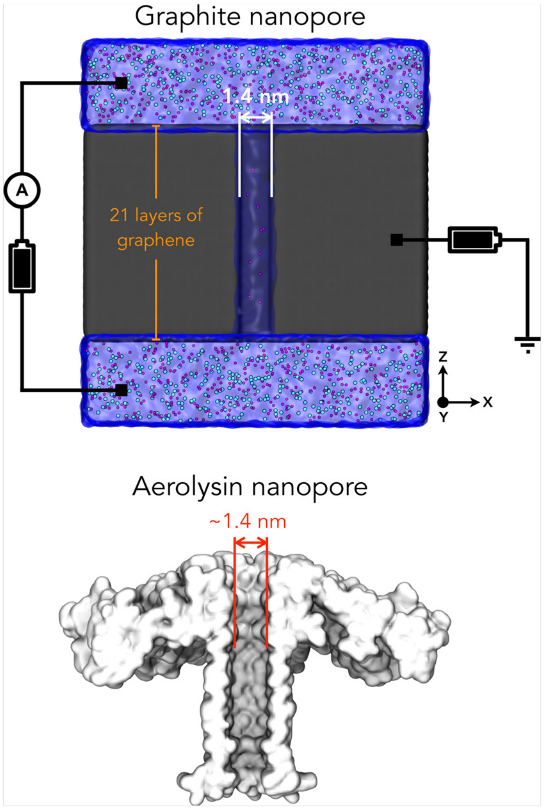

Fig. 1 Schematic representation of a graphite nanopore (top panel) inspired by the aerolysin biological nanopore (bottom panel) used in this study for glycan discrimination. The graphite nanopore was constructed by vertically stacking 21 layers of graphene, in which a nanopore with a diameter of 1.4 nm was opened. A negative voltage source, independent of the transmembrane voltage, was applied to the graphite material to render the nanopore negatively charged. The graphite nanopore was submerged in a 1 M KCl electrolyte solution. The graphite nanopore is shown in a gray cutaway molecular surface representation. K^+ and Cl^- ions are depicted as magenta and cyan spheres, respectively, while the transparent blue surface represents the aqueous environment. The structure of aerolysin, shown in a white cutaway molecular surface representation, was rendered from the molecular structure with ID 9FM6[7] in the PDB database.

2 Computational details

The proposed solid-state nanopore was constructed within a graphite membrane composed of 21 vertically stacked graphene layers, each measuring 10 nm × 10 nm, generated using the Carbon Nanostructure Builder plugin in VMD.[28]

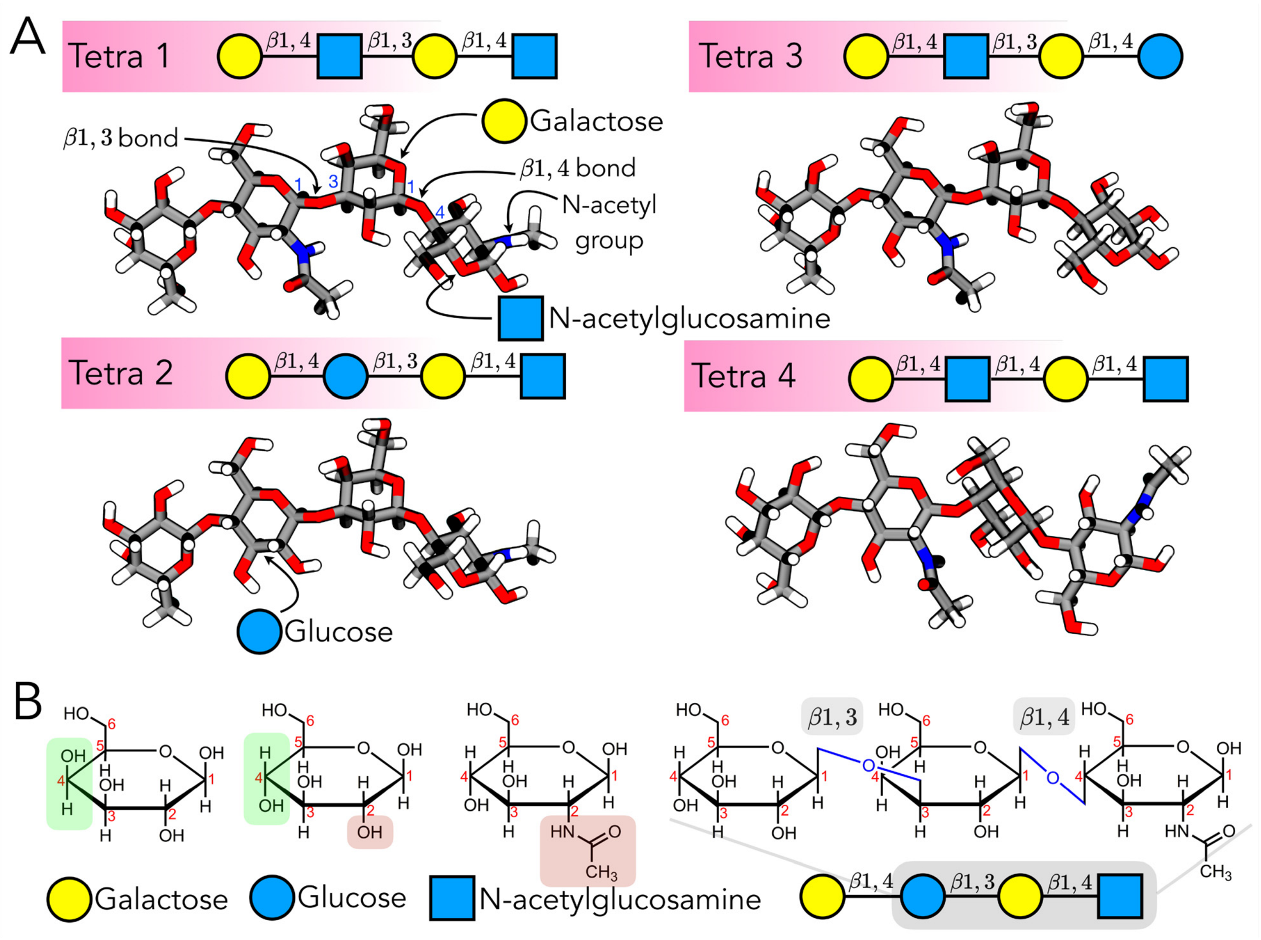

Fig. 2 (A) Four distinct tetrasaccharides, each consisting of two *N*-acetyl-lactosamines and differing in *N*-acetylation patterns and glycosidic linkage types, were studied here. The sequence of Tetra 1 is Galβ1,4-GlcNAcβ1,3-Galβ1,4-GlcNAc, Tetra 2 is Galβ1,4-Glcβ1,3-Galβ1,4-GlcNAc, Tetra 3 is Galβ1,4-GlcNAcβ1,3-Galβ1,4-Glc, and Tetra 4 is Galβ1,4-GlcNAcβ1,4-Galβ1,4-GlcNAc. Gal, Glc, and GlcNAc stand for galactose, glucose, and *N*-acetylglucosamine, respectively. Tetra 1 differs from Tetra 2 and Tetra 3 in the degree of *N*-acetylation, while Tetra 2 differs from Tetra 3 in the *N*-acetylation pattern. Galactose, glucose, and *N*-acetylglucosamine, along with β1,3 and β1,4 glycosidic bonds, are indicated in the figure, as well as the *N*-acetyl group of *N*-acetylglucosamine. (B) The chemical structures of galactose, glucose, and *N*-acetylglucosamine, as well as β1,3 and β1,4 glycosidic linkages, are shown. The stereoisomeric configuration of the hydroxyl groups in galactose and glucose is highlighted in green, while the *N*-acetyl group in *N*-acetylglucosamine (that differs from glucose) is highlighted in red. Glycosidic bonds are highlighted in blue, and atom numbers (in red) are indicated in the figures. The symbol-based representations of glycans through the circles and squares of different colors are consistently used throughout.

Subsequently, a circular nanopore was opened by removing all carbon atoms satisfying the condition $x^2 + y^2 < R^2$ where x and y denote the atomic coordinates and R is the target pore radius, resulting in a narrow, cylindrical nanopore with a diameter of 1.4 nm that closely resembles the pore architecture of the biological aerolysin nanopore; see schematic diagram of Fig. 1 in the main text for the bio-inspired graphite nanopore used for glycan detection. The graphite material was parameterized using the generalized Amber force field (GAFF),[29,30] while graphitic carbon atoms were treated as aromatic carbons (ca atom type) within the framework of GAFF. Following this, a partial charge of $-0.001e$ was assigned to each graphitic carbon atom, resulting in an overall negatively charged nanopore that generates a unidirectional water flow (*i.e.* EOF) induced by the pore lumen charge, thereby facilitating glycan translocation, as observed in the biological OmpF[18] nanopore. This charge was chosen in order to drive the glycan through the pore as it leads to parallel EOF and EPF. We have also tested the case of a higher charge density of the nanopore by setting the charge to $|0.002|e$/nanopore atom. In this case, though, the EOF and EPF are anti-parallel hindering the glycan movement. The nanopore was then placed in a simulation box measuring 10 nm × 10 nm × 11.5 nm, which was then filled with 16 920 TIP3P[31] water molecules. A total of 82 K^+ ions were added to neutralize the net charge of the negatively charged nanopore system. In addition, 723 K^+ and 723 Cl^- ions were introduced to achieve a 1 M KCl electrolyte solution, bringing the total number of atoms in the open nanopore system to 133 810. Periodic boundary conditions (PBC) were applied in all three directions.

Molecular Dynamics (MD) simulations of the graphite-based nanopore submerged in an aqueous 1 M KCl solution were conducted using the implementation in GROMACS[32] (version 2024.4). We begin the MD simulations with energy minimization of the system using the steepest descent algorithm. To maintain the structural integrity of the graphite material, harmonic position restraints with a force constant of 10 000 kJ mol^{-1} nm^{-2} were applied to all graphitic carbon atoms and maintained throughout the subsequent MD simulations. The system is subsequently equilibrated by raising the temperature from 0 K to 300 K over 1 ns under the canonical (NVT) ensemble. This was followed by a 5 ns equilibration under isobaric–isothermal (NPT) ensemble. The temperature was kept constant at 300 K using a velocity[33] rescaling thermostat with a coupling time constant of 0.1 ps. A semi-isotropic pressure coupling allowing independently coupling the lateral (xy) directions and the normal (z) direction to a pressure bath, was employed with a weak coupling Berendsen[34] barostat (time constant of 5 ps and compressibility of 4.5×10^{-5} bar^{-1}). This enabled equilibration of the system along the z direction under a constant pressure of 1 bar.

Non-bonded interactions, including van der Waals and electrostatic forces, were calculated using a buffered Verlet neighbor list.[35] Short-range interactions were computed directly up to a cutoff of 1.2 nm, with van der Waals potentials smoothly shifted to zero at the cutoff. Electrostatic interactions within the cutoff distance were calculated explicitly in real space, whereas interactions beyond the cutoff were treated using the Particle Mesh Ewald (PME)[36,37] method. The SETTLE algorithm[38] was used to constrain the internal degrees of freedom of water molecules, while the LINCS algorithm[39] constrained all bonds involving hydrogen atoms, allowing the system to be integrated using a 2 fs time step with the leap-frog algorithm. Following equilibration, production simulations are performed in the NVT ensemble under an applied electric field. The electric field strength (E) is defined as $E = V/l_z$, where V is the transmembrane voltage and l_z is the box length along z-axis.[40] We performed MD simulations (each 50 ns) under the voltages of −0.25 V, −0.5 V, −0.75 V, and −1.0 V to investigate how cumulative water fluxes are modulated by the applied transmembrane voltage. This simulation protocol was successfully established in our previous work.[19] Notably, ionic current measurements using a KCl electrolyte through a biological anthrax protective antigen nanopore have been reported to exhibit apparent fluctuations (*e.g.*, baseline drift and spurious signal interference), attributed to the Hofmeister effect.[41] In contrast, graphite nanopores appear to be completely immune to these effects, showing stable ionic current without such spurious fluctuations.

Four distinct tetrasaccharides (see Fig. 2), each consisting of two *N*-acetyl-lactosamines and differing in *N*-acetylation patterns and glycosidic linkage types were studied here. The sequence of Tetra 1 is Galβ1,4-GlcNAcβ1,3-Galβ1,4-GlcNAc, Tetra 2 is Galβ1,4-Glcβ1,3-Galβ1,4-GlcNAc, Tetra 3 is Galβ1,4-GlcNAcβ1,3-Galβ1,4-Glc, and Tetra 4 is Galβ1,4-GlcNAcβ1,4-Galβ1,4-GlcNAc. Gal, Glc, and GlcNAc stand for galactose, glucose, and *N*-acetylglucosamine, respectively. Tetra 1 differs from Tetra 2 and Tetra 3 in the degree of *N*-acetylation, while Tetra 2 differs from Tetra 3 in the *N*-acetylation pattern. Tetra 4 differs from Tetra 1 in the type of glycosidic linkage. Tetra 2 and Tetra 3, as well as Tetra 1 and Tetra 4, are structural isomers with identical mass. All glycan structures were constructed using the CHARMM-GUI[42] web server, and the AMBER compatible GLYCAM06[43] force field was used to parameterize the glycan molecules.

Starting from an equilibrated open nanopore system, a glycan molecule (Tetra 1), was positioned at the pore entrance by replacing approximately 5–6 water molecules per monosaccharide residue. Following energy minimization and a short equilibration, production simulations (50 ns each) were performed under applied transmembrane voltages of −0.25 V, −0.5 V, −0.75 V, and −1.0 V. During the equilibration phase, a harmonic positional restraint (with a force constant of 1000 kJ mol^{-1} nm^{-2}) was applied to the hydroxyl O atom at the C1 position of the first monosaccharide residue. Later, the positional restraint on the glycan molecule was removed during the production runs, allowing the glycan to freely translocate through the nanopore under the joint influence of the applied electric field and water flux. Even after several occurrences of spontaneous translocation, the events are too few to yield statistically reliable estimates of ionic current blockade, therefore we adopted an alternative strategy. An umbrella restraint (with a spring constant of 1000 kJ mol^{-1} nm^{-2}) was introduced between the center of mass (COM) of atoms at the pore entrance and the hydroxyl O atom at the C1 position of the first monosaccharide residue; see SI Fig. S1. This restraint was found sufficient to hold the glycan in the pore. However, all other atoms in the glycan were free to move.

The restraint effectively maintained the glycan in a configuration corresponding to partial translocation (approximately halfway into the pore), with an indefinite residence time. This approach enables sufficient sampling of ionic current blockades in the presence of the glycan, thereby significantly improving the accuracy of glycan discrimination. Notably, the restrained ‘hanging’ glycan configuration, maintained by a harmonic spring with an indefinite residence time, also serves as a model for experimentally captured glycan using phenylboronic acid adapter within biological nanopores.[8,16] Similar to Tetra 1, the other tetrasaccharides (namely, Tetra 2, Tetra 3 and Tetra 4), as well as the pentasaccharide (namely, Penta) and hexasaccharide (namely, Hexa), were placed at the halfway along the nanopore and restrained by a harmonic spring constant. All voltage-biased MD simulations with glycans were performed under an applied transmembrane voltage of −1.0 V. For each glycan, 15 independent MD simulations of 50 ns each were conducted, with distinct random seeds used to initialize atomic velocities. This resulted in a total accumulated trajectory length of 750 ns per system for mean ionic current[40] analysis and the distribution of the charge density around the glycan molecule.

3 Results and discussion

3.1 Water flux driven glycan translocation

We begin the analysis of the MD simulations by assessing the modulation of the water flux associated with the EOF within a negatively charged graphite nanopore under varying applied transmembrane voltages. For this, we considered a graphite nanopore submerged in a 1 M KCl electrolyte solution and connected to a negative voltage source, thereby rendering the nanopore negatively charged. An independent transmembrane voltage was applied across the membrane to drive ion transport through the nanopore. Under −1.0 V transmembrane potential, the negatively charged graphite nanopore exhibits a purely cation-conducting behavior, as reflected by the cumulative individual ion fluxes of K^+ and Cl^- ions. No notable Cl^- transport through the pore was observed over the entire simulation time. The K^+ ion flux induces a huge water flux in the same direction as the applied electric field (Fig. 3A). Subsequently, we varied the applied transmembrane voltage from −1.0 V to −0.25 V in steps of −0.25 V and monitored the cumulative water flux under each biased potential. Interestingly, the cumulative water flux decreases as the transmembrane potential is reduced from −1.0 V to −0.25 V, indicating that the magnitude of EOF can be precisely modulated by tuning the applied transmembrane voltage (Fig. 3B). It is worth noting that the present negatively charged graphite nanopore setup can be viewed as analogous to a nanofluidic pnp-type transistor,[44,45] exhibiting current amplification behavior (SI Fig. S2 and S3), where positive charge carriers dominate the transport from the emitter to the collector.

Following this, we investigated the EOF-driven translocation of a glycan through the nanopore. To this end, a glycan molecule (Tetra 1) was placed at the entrance of the nanopore and allowed to translocate freely (Fig. 3C) along the pore under

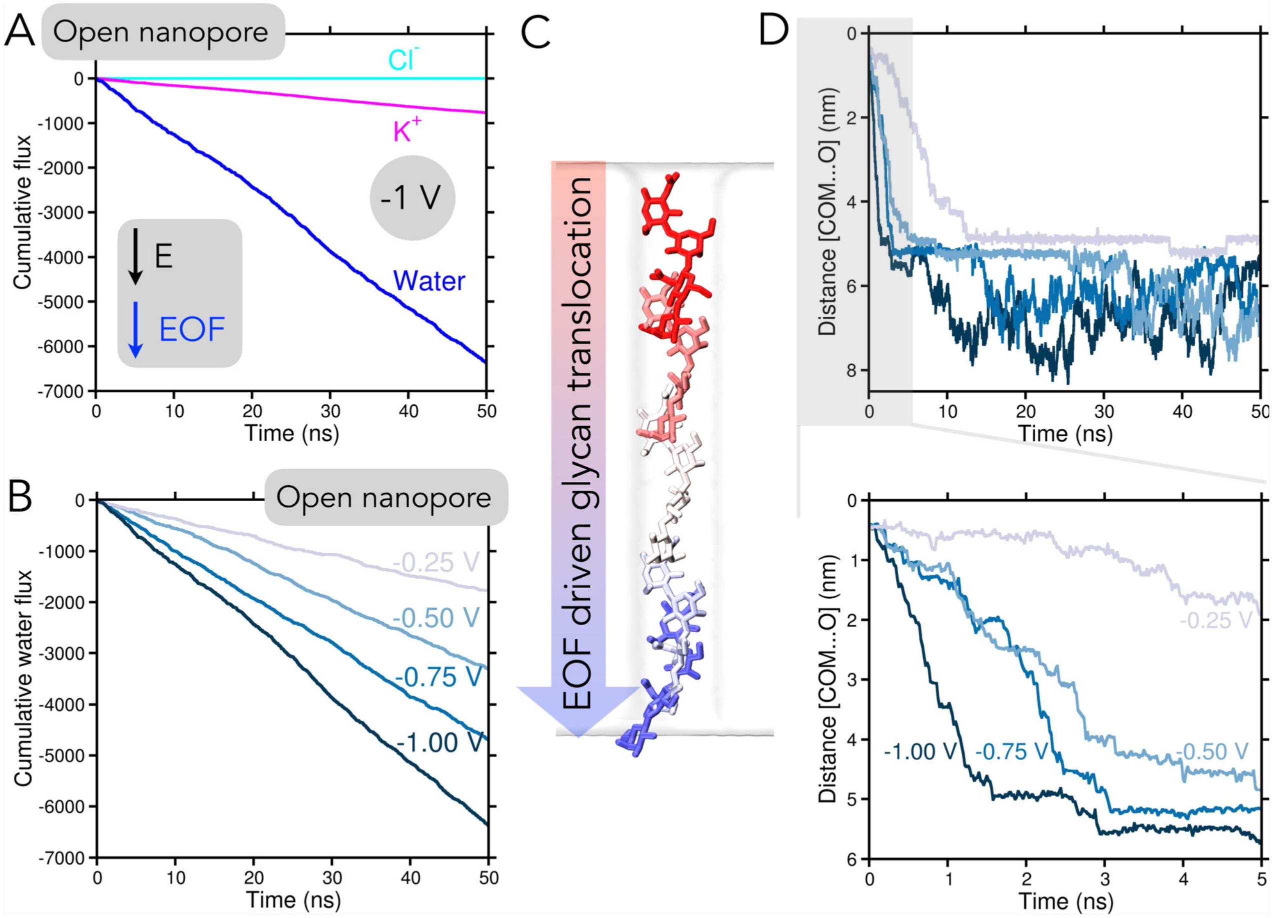

Fig. 3 Water flux driven glycan translocation. (A) Cumulative flux of the ions and water through the open nanopore under a transmembrane voltage of −1 V. The species are color-coded as defined in the labels. The directions of the applied transmembrane electric field (*E*) and the electro-osmotic flow (EOF) are indicated. (B) Cumulative water flux under different transmembrane voltages, demonstrating modulation of water transport by the applied voltage. (C) Representative MD snapshot illustrating water flux driven glycan translocation through the nanopore. The start and end of the translocation process is depicted using a color gradient from red to blue, respectively. (D) In the top panel, the time evolution of the distance between the center of mass (COM) of the pore entrance atoms and the hydroxyl O atom at the C1 position of the first monosaccharide unit of the glycan is shown. A zoomed-in view of the initial 5 ns (gray box in the top panel) of the translocation event is shown in the bottom panel, emphasizing the variation in the extent of the translocation with the applied transmembrane voltage.

applied transmembrane voltages of −1.0 V, −0.75 V, −0.50 V, and −0.25 V. Translocation events were successfully observed at all four transmembrane voltages, with the timescale of the translocation process varying significantly with the applied voltage, as evident from the dynamics of the glycan distance (hydroxyl O atom at the C1 position of the first monosaccharide unit) to the pore entrance (and its center of mass, COM) shown in (Fig. 3D). Glycan translocation was fastest at −1.0 V and slowest at −0.25 V, with typical dwell times (defined as the time required for the hydroxyl O atom to traverse 6 nm from the COM) of approximately 8 ns at −1.0 V, 15 ns at −0.75 V, 34 ns at −0.5 V, and more than 50 ns at −0.25 V. This trend is consistent with the magnitude of the water flux under applied voltages, as shown in Fig. 3B, indicating that adjusting the applied transmembrane voltage controls EOF-driven glycan translocation and, in turn, the dwell time of glycans within the nanopore. To further support this observation, we carried out translocation simulations at −1.0 V using a charge-neutral nanopore, under which no translocation was observed (SI Fig. S4). EOF-driven glycan translocation has also been reported previously in the case of OmpF biological nanopore in which the intrinsic EOF generates a robust driving force for the translocation of unlabeled, neutral oligosaccharides.[18]

3.2 Glycan discrimination

Despite multiple occurrences of spontaneous translocation events, it might be insufficient to obtain statistically robust estimation of ionic current blockades within the simulation timescale. To circumvent this limitation, we have adopted an alternative strategy; an umbrella restraint was introduced between the center of mass (COM) of atoms at the pore entrance and the hydroxyl O atom at the C1 position of the first monosaccharide residue (SI Fig. S1). This restraint effectively maintained the glycan in a partially translocated configuration – approximately halfway into the pore, with an indefinite residence time. This approach enabled sufficient sampling of ionic current blockades in the presence of the glycan. The strategy described above can be viewed as analogous to capturing glycans using phenylboronic acid adapter within biological nanopores,[8,16,17] which prolongs the glycan dwell time and enables their accurate detection. This further hints at the possibility of functionalizing the graphite nanopore with phenylboronic acid. However, this possibility is not explored in the present study. Employing this restraint simulation setup, we were able to discriminate glycans with different degrees of *N*-acetylation, distinct *N*-acetylation patterns, and different glycosidic linkages. Notably, the latter two classes correspond to structural isomers with identical molecular masses. Furthermore, we extended glycan discrimination to species with different degrees of polymerization by gradually increasing the number of monosaccharide units in the glycan chain. The following sections provide a detailed discussion of these findings. Note that, all simulations were performed under an applied transmembrane voltage of −1.0 V, at which the highest ionic current was observed. Although faster spontaneous translocation events were also found at −1.0 V, the primary motivation for this choice was a high ionic current, which enables more accurate estimation of current blockades by reducing statistical uncertainty. Although our proof-of-principles observations are very promising, a direct comparison to relevant experiments[10] is not possible due to significant differences in pore materials and translocation conditions. In a broad sense, structurally distinct tetrasaccharides, as well as pentasaccharide, and hexasaccharide are expected to exhibit characteristic ionic current regimes in experimental measurements. The objective of this work was to provide molecular-level insights fully utilizing the simulations. These aim to initiate and motivate relevant experimental work.

3.2.1 Different degrees of *N*-acetylation. In view of glycan detection, we first aimed to differentiate two glycan chains with distinct degrees of *N*-acetylation. To this end, we analyzed two glycans, Tetra 1 and Tetra 2. In Tetra 1, the third monosaccharide unit is *N*-acetylglucosamine, whereas in Tetra 2, it is replaced by glucose (Fig. 4A). This subtle steric difference is expected to be reflected in the ionic current recordings. Indeed, the mean blockade current for Tetra 1 differs from that of Tetra 2, with Tetra 1 exhibiting a slightly lower mean current. To delineate the molecular mechanism underlying the differences in ionic current traces, we analyzed the charge density distribution around the glycan within the pore lumen. Not only does the confinement of the glycan within the pore naturally introduce a nonuniform charge distribution, but steric effects also impede ion flow, thereby reducing the local charge density around the moiety. Using Tetra 1 as a reference, an evident difference in charge density is observed at the position of the third monosaccharide, where Tetra 1 contains *N*-acetylglucosamine and Tetra 2 contains glucose. In Tetra 2, more ions flow around the glucose residue due to the absence of the *N*-acetyl group present in *N*-acetylglucosamine, thereby enhancing the charge density. In the same vein, we also analyzed Tetra 1 and Tetra 3, in which the first residue in Tetra 1 is a *N*-acetylglucosamine, whereas it is a glucose in Tetra 3. A distinct difference in blockade current was observed between the two species, accompanied by a difference in local charge density (SI Fig. S5). These results underpin the capability of the graphite nanopore to distinguish glycans with different *N*-acetylation degrees.

3.2.2 Different *N*-acetylation pattern. We next extend our glycan detection strategy to glycans that differ in their *N*-acetylation patterns, *i.e.*, in the relative positions of *N*-acetylglucosamine and glucose residues along the chain. Notably, these glycans have identical molecular masses but are distinct structural isomers. Identifying structural isomers with the same mass is inherently challenging using mass spectrometry; in most cases, such distinctions require NMR spectroscopy. Similar challenges were also reported in the diagnosis of PTMs in proteins.[24] To this end, we considered two glycan chains, Tetra 2 and Tetra 3. In Tetra 2, the first monosaccharide residue is *N*-acetylglucosamine, which is replaced by glucose in Tetra 3; conversely, the third *N*-acetylglucosamine residue in Tetra 3 is replaced by glucose in Tetra 2 (Fig. 4B). The blockade currents of Tetra 2 and Tetra

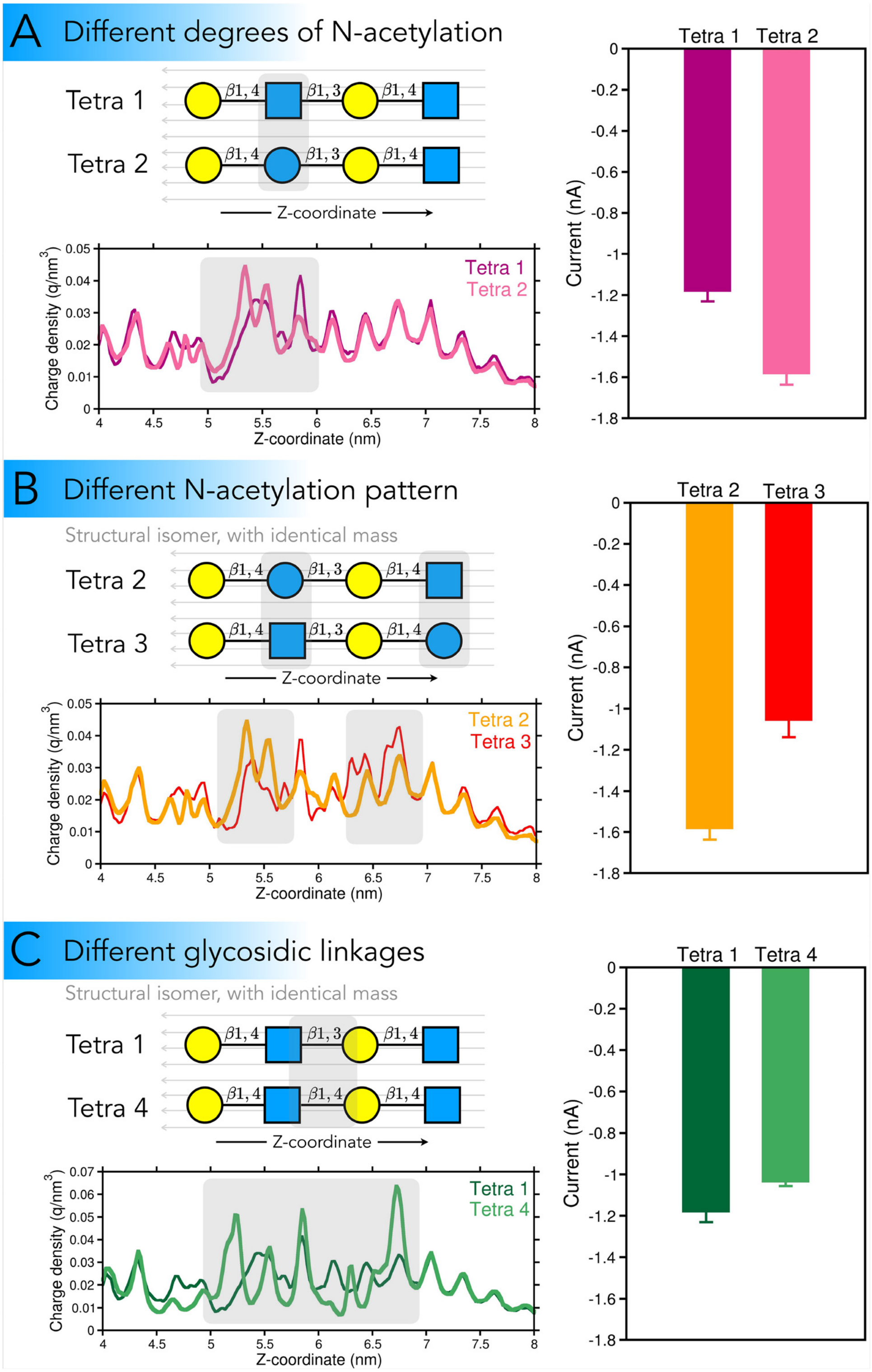

Fig. 4 Discrimination of glycans with different degrees of *N*-acetylation (panel A), different *N*-acetylation patterns (panel B), and different glycosidic linkages (panel C). Symbol-based representations of Tetra 1, Tetra 2, Tetra 3, and Tetra 4 are shown as defined in Fig. 2. Thin light gray arrows indicate the direction of cation flow, as the negatively charged nanopore conducts cations exclusively. Calculated nanopore ionic currents for the tetrasaccharides, with associated uncertainties, are presented along with charge density distributions around the glycan within the pore lumen. The structural differences between the two tetrasaccharide units, as well as the corresponding differences in charge density, are highlighted in light gray.

3 show a significant difference. This can be rationalized by variations in the charge density distribution around the glycans, arising from differences in their molecular shape. Notably, in Tetra 2, the *N*-acetyl group on the first *N*-acetylglucosamine residue introduces steric hindrance to the ion flow, thereby lowering the local charge density. In contrast, in Tetra 3 the *N*-acetyl group is located on the third residue, resulting in a charge density distribution that is mirrored relative to Tetra 2.

3.2.3 Different glycosidic linkages. Following the successful detection of structurally isomeric glycans with different *N*-acetylation patterns, we probe the potential of the negatively charged graphite nanopore in differentiating two glycans with distinct glycosidic bonds (Fig. 4C). Structural isomers, which arise from variations in glycosidic linkages, are ubiquitous and pose considerable difficulties for glycan analysis. In Tetra 1, the second glycosidic bond between galactose and *N*-acetylglucosamine is a β1,3 linkage, whereas in Tetra 4, the same bond is a β1,4 linkage. Otherwise, the two glycans are identical, and are thereby expected to produce nearly identical blockade currents. Indeed, the mean blockade currents of Tetra 1 and Tetra 4 are not significantly different, though their subtle differences can be resolved at pA-resolution. As glycosidic linkages govern the molecular conformation of glycans, the charge accumulation around the glycans within the pore also differs.

3.2.4 Different degrees of polymerization. Finally, we extended the applicability of the graphite nanopore to discriminate glycans with different chain lengths. To this end, tetrasaccharide glycan chains were extended to hexasaccharides by alternately adding *N*-acetylglucosamine and galactose units (Fig. 5A). As expected, increasing the chain length further impedes ion flow, resulting in a gradual decrease in the mean blockade current – highest for Tetra 1, intermediate for Penta, and lowest for Hexa (Fig. 5B). These data indicate an overall linear correlation between current blockades and glycan chain length. Besides this, in biology, glycans are also found with two or more branches, which are not considered in the present study. Nonetheless, graphite nanopores hold significant promise for their detection. Realizing this potential will involve the development of nanopore with larger pore diameters, motivating follow up investigation. Furthermore, functionalization of graphite nanopore with Lewis acids, such as a phenylboronic acid, in combination with EOF-facilitated translocation, could substantially expand the applicability of nanopore sensing to other carbohydrates, particularly monosaccharides, as well as to other small-molecule analytes with high precision.

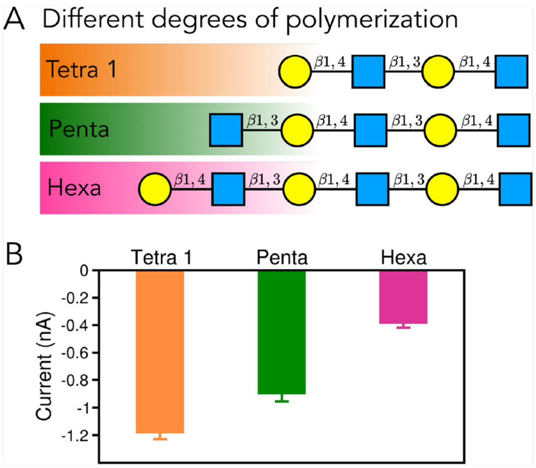

Fig. 5 Identifying glycans with varying degrees of polymerization. (A) Symbol-based representations from tetrasaccharides to hexasaccharides, and (B) their blockade ionic currents.

4 Concluding remarks

In closing, this computational investigation demonstrates the capability of negatively charged graphite nanopores for single-molecule glycan detection. Under an applied transmembrane voltage, the negatively charged nanopore generates EOF, which drives glycan translocation and provides a label-free approach for transporting these charge-neutral molecules through the nanopore. Building upon this, we systematically elucidated the discrimination of various glycan molecules, including differences in the number of *N*-acetylations, distinct *N*-acetylation patterns, and even regioisomeric configurations. These complex yet subtle structural compositional differences give rise to distinct ionic current responses, resolved in the pA-region, which are in fact traced to species-dependent charge accumulation within the nanopore lumen. In fact, the glycan differentiation was extended to glycans of varying chain lengths.

Similar to biological pores, solid-state nanopores such as the graphite material proposed here show a high potential in glycan read-out. The latter additionally provides a higher material stability and ease in functionalization, which would in turn provide an additional mode in enhancing the discrimination possibly also beyond the pA range. At the same time, tuning the EOF-guided translocation in order to enhance the sensing accuracy can be achieved by adjusting the interplay of the transmembrane electric field to the charging of the material, a fairly simple approach compared to strategies (such as pore engineering and mutations) followed in biological nanopores. With this study, we aimed to explore – for the first time – the potential of solid-state nanopores in glycan detection. Accordingly, this is the first step towards the realization of glycan detection with selective solid-state nanopores. Beyond the molecular-level proof-of-principles insights provided here, follow-up computational studies should further explore this potential to investigate mixtures of analytes, the capture of the molecules to the pore, translocation kinetics, *etc.* and at the same time complement with parallel experimental studies. Taken together, this work underscores the potential of graphite nanopores for high-resolution carbohydrate analysis and paves the way for the future development of glycan sequencing using solid-state-based nanopores.

Author contributions

Chandan K. Das: conceptualization, investigation, formal analysis, resources, and writing – original draft, review and editing. Maria Fyta: funding acquisition, resources, supervision, and writing – review and editing.

Conflicts of interest

There are no conflicts to declare.

Data availability

The data generated and analyzed in this work can be made available upon any reasonable request. The supporting data has been also provided as part of the supplementary information (SI). Supplementary information: measurements of open nanopore currents under various applied voltages, ionic pnp-type transistor, glycan translocation through a neutral nanopore, and the discrimination of glycans, namely Tetra 1 and Tetra 3. See DOI: https://doi.org/10.1039/d6nr00916f.

Acknowledgements

The authors acknowledge the computing time provided by the NHR Center NHR4CES at RWTH Aachen University (project number p0022407). This computing support was funded by the Federal Ministry of Education and Research and the participating state governments, in accordance with the resolutions of the GWK for national high-performance computing at universities. This work is part of the nanodiagBW consortium (project number 03ZU1208BI), funded by the German Federal Ministry of Education and Research (BMBF) within the Clusters4Future initiative. The authors also gratefully acknowledge funding from the German Research Foundation (Deutsche Forschungsgemeinschaft, DFG; project number 508324943).

References

1 *Essentials of Glycobiology*, ed. A. Varki, R. D. Cummings and J. D. Esko, *et al.*, Cold Spring Harbor Laboratory Press, Cold Spring Harbor, NY, 4th edn, 2022.

2 S. S. Shivatare, V. S. Shivatare and C.-H. Wong, *Chem. Rev.*, 2022, **122**, 15603–15671.

3 C. Anish, M. Beurret and J. Poolman, *npj Vaccines*, 2021, **6**, 150.

4 B. A. H. Smith and C. R. Bertozzi, *Nat. Rev. Drug Discovery*, 2021, **20**, 217–243.

5 L. Pan, C. Cai, C. Liu, D. Liu, G. Li, R. J. Linhardt and G. Yu, *Curr. Opin. Biotechnol.*, 2021, **69**, 191–198.

6 Y.-L. Ying, Z.-L. Hu, S. Zhang, *et al.*, *Nat. Nanotechnol.*, 2022, **17**, 1136–1146.

7 J. S. Anton, I. Iacovache, J. F. Bada Juarez, L. A. Abriata, L. W. Perrin, C. Cao, M. J. Marcaida, B. Zuber and M. Dal Peraro, *J. Am. Chem. Soc.*, 2025, **147**, 4984–4992.

8 W. J. Ramsay and H. Bayley, *Angew. Chem., Int. Ed.*, 2018, **57**, 2841–2845.

9 B. Xia, J. Fang, S. Ma, M. Ma, G. Yao, T. Li, X. Cheng, L. Wen and Z. Gao, *J. Am. Chem. Soc.*, 2023, **145**, 18812–18824.

10 G. Yao, Y. Tian, W. Ke, J. Fang, S. Ma, T. Li, X. Cheng, B. Xia, L. Wen and Z. Gao, *J. Am. Chem. Soc.*, 2024, **146**, 13356–13366.

11 G. Yao, B. Xia, F. Wei, J. Wang, Y. Yang, S. Ma, W. Ke, T. Li, X. Cheng, L. Wen, Y.-t. Long and Z. Gao, *J. Am. Chem. Soc.*, 2025, **147**, 1721–1731.

12 M. Li, Y. Xiong, Y. Cao, *et al.*, *Nat. Commun.*, 2023, **14**, 1737.

13 P. Bayat, C. Rambaud, B. Priem, *et al.*, *Nat. Commun.*, 2022, **13**, 5113.

14 M. Li, J. Wang, C. Zhang, X. Zhao, Y. Xiong, Y. Cao, D. Wang, X. Li, X. Liang and G. Qing, *ACS Nano*, 2024, **18**, 25155–25169.

15 S. Zhang, Z. Cao, P. Fan, Y. Wang, W. Jia, L. Wang, K. Wang, Y. Liu, X. Du, C. Hu, P. Zhang, H.-Y. Chen and S. Huang, *Angew. Chem., Int. Ed.*, 2022, **61**, e202203769.

16 S. Zhang, Z. Cao, P. Fan, W. Sun, Y. Xiao, P. Zhang, Y. Wang and S. Huang, *Angew. Chem., Int. Ed.*, 2024, **63**, e202316766.

17 X. Gao, Y. Xiao, W. Li, L. Qian, K. Wang, P. Zhang and S. Huang, *Nano Lett.*, 2026, **26**, 74–82.

18 F. Gao, J.-H. Wang, H. Ma, B. Xia, L. Wen, Y.-T. Long and Y.-L. Ying, *Angew. Chem., Int. Ed.*, 2025, **64**, e202422118.

19 C. K. Das and M. Fyta, *Small*, 2025, **21**, 2407647.

20 S. Mittal, M. K. Jena and B. Pathak, *ACS Cent. Sci.*, 2024, **10**, 1689–1702.

21 S. Mittal, M. K. Jena and B. Pathak, *ACS Appl. Eng. Mater.*, 2025, **3**, 2441–2454.

22 C. Lu, A. Bonini, J. H. Viel and G. Maglia, *Nat. Biotechnol.*, 2025, **43**, 312–322.

23 L. Xue, H. Yamazaki, R. Ren, M. Wanunu, A. P. Ivanov and J. B. Edel, *Nat. Rev. Mater.*, 2020, **5**, 931–951.

24 T. Ensslen, K. Sarthak, A. Aksimentiev and J. C. Behrends, *J. Am. Chem. Soc.*, 2022, **144**, 16060–16068.

25 L. Bacri, A. Oukhaled, E. Hémon, F. B. Bassafoula, L. Auvray and R. Daniel, *Biochem. Biophys. Res. Commun.*, 2011, **412**, 561–564.

26 M. Shankla and A. Aksimentiev, *J. Phys. Chem. B*, 2017, **121**, 3724–3733.

27 M. Tsutsui, W.-L. Hsu, D. Garoli, I. W. Leong, K. Yokota, H. Daiguji and T. Kawai, *ACS Nano*, 2024, **18**, 15046–15054.

28 W. Humphrey, A. Dalke and K. Schulten, *J. Mol. Graphics*, 1996, **14**, 33–38.

29 J. Wang, R. M. Wolf, J. W. Caldwell, P. A. Kollman and D. A. Case, *J. Comput. Chem.*, 2004, **25**, 1157–1174.

30 X. Dong, X. Yuan, Z. Song and Q. Wang, *Phys. Chem. Chem. Phys.*, 2021, **23**, 12582–12591.

31 P. Mark and L. Nilsson, *J. Phys. Chem. A*, 2001, **105**, 9954–9960.

32 *SoftwareX*, 2015, **1–2**, 19–25.

33 G. Bussi, D. Donadio and M. Parrinello, *J. Chem. Phys.*, 2007, **126**, 014101.

34 H. J. C. Berendsen, J. P. M. Postma, W. F. van Gunsteren, A. DiNola and J. R. Haak, *J. Chem. Phys.*, 1984, **81**, 3684–3690.

35 S. Páll and B. Hess, *Comput. Phys. Commun.*, 2013, **184**, 2641–2650.

36 T. Darden, D. York and L. Pedersen, *J. Chem. Phys.*, 1993, **98**, 10089–10092.

37 U. Essmann, L. Perera, M. L. Berkowitz, T. Darden, H. Lee and L. G. Pedersen, *J. Chem. Phys.*, 1995, **103**, 8577–8593.

38 S. Miyamoto and P. A. Kollman, *J. Comput. Chem.*, 1992, **13**, 952–962.

39 B. Hess, C. Kutzner, D. van der Spoel and E. Lindahl, *J. Chem. Theory Comput.*, 2008, **4**, 435–447.

40 A. Aksimentiev, J. B. Heng, G. Timp and K. Schulten, *Biophys. J.*, 2004, **87**, 2086–2097.

41 J. Li, Y. Wang, L. Wang, Y. Wang, Z. Zhang, S. Liu and L. Wang, *ACS Mater. Lett.*, 2025, **7**, 2476–2481.

42 S. Jo, T. Kim, V. G. Iyer and W. Im, *J. Comput. Chem.*, 2008, **29**, 1859–1865.

43 K. N. Kirschner, A. B. Yongye, S. M. Tschampel, J. González-Outeiriño, C. R. Daniels, B. L. Foley and R. J. Woods, *J. Comput. Chem.*, 2008, **29**, 622–655.

44 Y.-L. Hu, Y. Hua, Z.-Q. Pan, J.-H. Qian, X.-Y. Yu, N. Bao, X.-L. Huo, Z.-Q. Wu and X.-H. Xia, *Nano Lett.*, 2022, **22**, 3678–3684.

45 T. Mei, W. Liu, G. Xu, Y. Chen, M. Wu, L. Wang and K. Xiao, *ACS Nano*, 2024, **18**, 4624–4650.